ACS NANO

www.acsnano.org

ARTICLE

Photoluminescence from Metal Nanostructures: Dependence on Size

Imon Kalyan, Ieng Wai Un, Gilles Rosolen, Nir Shitrit, and Yonatan Sivan*

Cite This: *ACS Nano* 2025, 19, 29181−29194

Read Online

ACCESS | Metrics & More | Article Recommendations | Supporting Information

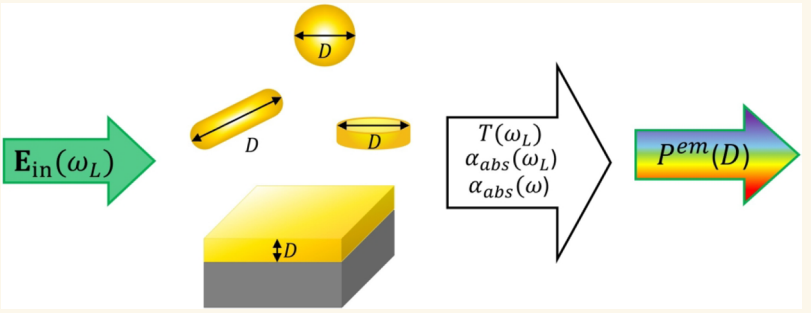

ABSTRACT: **For decades, there have been multiple seemingly contradicting experimental reports on the dependence of the photoluminescence (PL) from metal nanostructures on their size. We reconcile these reports using a simple analytical formula that is found to match PL measurements well for a range of structures and illumination conditions. Our expression requires only knowledge of the local electric field and temperature and points to the physical quantities that determine the emission strength and its dependence on the size.**

KEYWORDS: *plasmonics, photoluminescence, nonthermal charge carriers, electron nonequilibrium, fluctuation−dissipation theorem*

1. INTRODUCTION

The emission of light from metal nanostructures induced by illumination, frequently termed colloquially metal photoluminescence (PL), is a fundamental process occurring in a prototypical solid-state system. It also has practical importance; metal nanoparticles are frequently used as nonbleaching fluorescent labels in bioimaging,[1−3] correlative light-electron microscopy,[4] and more recently, as enablers of thermometry.[5−9]

Despite this dual importance, it is surprising that many aspects of the metal PL have been under debate for decades. These debates are on, for example, whether the emission occurs due to recombination of an electron and hole residing both within the conduction band[10−12] or involving a hole in the valence band (e.g., refs 13−18), on whether the emission statistics is Fermionic or bosonic (e.g., refs 7,19), thermal or nonthermal (e.g., refs 11,12,20−22), or how it depends on the local electric field (e.g., refs 11,20,21,23). Of particular interest is the dependence on the size of the nanostructure (e.g., refs 16,17,24−26). Many early studies studied the emission from metal clusters or few nm particles, primarily focusing on atomistic considerations and ligand coverage; these studies highlighted the trade-off between the presence of a plasmonic resonance and the quantum yield for emission, see ref 27. For larger structures, there have been reports of contradicting trends. For example, Dulkeith et al.[24] showed that the (time and) frequency integrated Stokes emission (SE) from spheres of growing radii illuminated by a short pulse scales linearly with their volume; similar results were reported by Gaiduk et al.[25] for continuous wave (CW) illumination. On the other hand, Lin et al.[28] and more recently, Bowman et al.[29] have demonstrated that the CW PL from rods and thin Au films, respectively, decreases with growing thickness; similar trends were reported in refs 17,30 for pulsed illumination. Other studies reported a mixed trend (e.g., ref 26).

These debates originate from the different conditions under which the PL measurements have been made (in terms of the number, density and shape of the nanostructure geometry, the illumination duration, intensity and wavelength, the relative position of the latter with respect to the resonances of the structure, the relative spectral position of emission with respect

Received: February 18, 2025
Revised: July 14, 2025
Accepted: July 16, 2025
Published: August 8, 2025

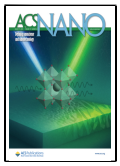

https://doi.org/10.1021/acsnano.5c02977
ACS Nano 2025, 19, 29181−29194

to the illumination wavelength, the geometry and thermal properties of the surrounding, etc.) or the exact quantity studied (temporally and/or spectrally resolved/integrated PL), but also from the absence of a simple theory that encompasses both photonic aspects of the problem (via the photonic density of states, as appearing in Purcell's formula, see e.g., ref 22), as well as the thermal aspects and the electronic aspects, that is, the distribution and associated weights of the continuum of possible recombination transitions.

Recently, Dubi and Sivan employed a simple analytical expression for the steady-state electron distribution in a Drude metal to derive an equally simple expression for the PL from metals illuminated by CW light.[12] By relying on the empiric values of the permittivity to determine the absorption, this approach circumvents the need to specify the transition matrix element and circumvents the arguments about the origins of the emission (being radiative recombination or electronic Raman/inelastic light scattering, etc.[5,29,31−34]). This predicted behavior was verified experimentally in ref 18 and enabled the resolution of many of the disagreements described above (in particular, associated with the emission statistics and electric-field dependence). This expression was more recently extended to explain the dependence of the PL following short pulse illumination on the electric field.[35]

In this work, we use the approach of ref 12 to reconcile the various seemingly contradicting reports on the size-dependence of the PL from the prototypical geometries of metal particles and films. Specifically, in Section 2, we combine the analytical expression of ref 12 with the detailed analysis of the heating of illuminated metal spheres[36] and most importantly, with recent progress made by Loirette-Pelous and Greffet, who showed how to determine the total PL of a metal nanostructure in the case of a nonthermal distribution.[37]

In Section 3, we use the resulting analytical expression to compute the PL from metal nanospheres and nanofilms as a function of their size. We distinguish between three cases. For weak illumination (hence, negligible heating), the dependence of the PL spectrum (both the Stokes Emission (SE) and the anti-Stokes Emission (aSE)) on the structure size is determined by a single parameter, the absorption cross-section density (or equivalently, via Kirchhoff's Law, the emission cross-section density); the electronic contribution is size-independent in this regime. Thus, generically, the PL scales with the *illuminated* volume; that is, it is a volume effect for small sizes and it becomes a surface effect when the size exceeds the penetration depth of a few 10s of nm. However, in the latter case, the resonances characteristic of particles modify further the size-dependence of the PL and effectively dominate it. Indeed, a change of size causes the emission at a given frequency to shift in and then out of resonance.

For stronger illumination (hence, moderate heating), the size-dependence of the PL is amplified through the dependence of the Bose function on the (electron) temperature. This has a fairly small effect on the SE, but a large effect on the aSE due to the exponential dependence of the Bose function on the temperature, which itself scales with the absorption cross-section density. For even stronger heating, thermo-optic effects kick in and cause the quality factor of the resonance to decrease.[38,39] This causes weaker (excessive) heating at resonance (away from resonance) and, hence, has a complex effect on the PL, depending on the emission frequency (SE/aSE).

We then demonstrate a good *qualitative* match between the prediction of our model and the experimental results for spheres and films; in fact, good *quantitative* matches are observed in most cases. We demonstrate different trends by looking also at other particle shapes (rods and nano disks) and find a good qualitative match, even in the presence of modest field and temperature nonuniformity levels. Remarkably, the agreement usually extends beyond the formal limits of the analysis, specifically, in the presence of interband emission events, which are not accounted for in our analytical expression.

In Section 4, we discuss possible reasons for the occasional quantitative mismatches we observe, the implications of the results, their pros and cons compared with more sophisticated approaches in the literature, specifically, the rigorous momentum-space calculations provided in refs 29,30,33, and mention possible extensions of our approach.

2. THEORY

In this section, we lay the theoretical foundation for the study of PL from various metal nanostructures. In many cases, the term photoluminescence is used to refer to spontaneous emission/radiative recombination of an electron and a hole, in contrast to inelastic light scattering, also known as electronic Raman scattering. In that sense, in this work, we use the term PL as a shorthand for emission, without distinguishing between these possibilities.

2.1. A Microscopic View. Based on the CW solution for f (the steady-state electron distribution) obtained in refs 40,41 for uniformly illuminated Drude metals and its experimental verification in refs 42−45, in ref 12, Sivan and Dubi presented a quantitative theory for the PL from Drude metals under CW illumination, showing that the *probability* of emitted photons per unit frequency is given approximately by

$$\Gamma^{\mathrm{em}}(\mathbf{r},\ \omega,\ \omega_{\mathrm{L}};\ \mathcal{E}_{\mathrm{F}}) \cong \gamma_{\mathcal{E}}(\mathbf{r},\ \omega,\ \omega_{\mathrm{L}};\ \mathcal{E}_{\mathrm{F}})\rho_{\mathrm{e}}^{2}(\mathcal{E}_{\mathrm{F}})I_{\mathrm{e}}(\omega,\ \omega_{\mathrm{L}},\ |\mathbf{E}_{\mathrm{L}}(\omega_{\mathrm{L}},\ \mathbf{r})|^{2}) \tag{1}$$

where

$$I_{\mathrm{e}}(\omega,\ \omega_{\mathrm{L}},\ |\mathbf{E}_{\mathrm{L}}(\omega_{\mathrm{L}},\ \mathbf{r})|^{2}) = \int f(\mathcal{E}+\hbar\omega,\ |\mathbf{E}_{\mathrm{L}}(\omega_{\mathrm{L}},\ \mathbf{r})|^{2})\,[1-f(\mathcal{E},\ |\mathbf{E}_{\mathrm{L}}(\omega_{\mathrm{L}},\ \mathbf{r})|^{2})]\mathrm{d}\mathcal{E} \tag{2}$$

represents the electronic contribution to the emission formula and

$$\gamma_{\mathcal{E}}(\mathbf{r},\ \omega,\ \omega_{\mathrm{L}},\ \mathcal{E}) = \frac{\pi\omega_{\mathrm{L}}V^{2}}{\epsilon_{0}}\left|\vec{\mu}(\mathcal{E},\ \mathcal{E}+\hbar\omega_{\mathrm{L}})\right|^{2}\rho_{\mathrm{phot}}(\mathbf{r},\ \omega) \tag{3}$$

represents the emission rate of a single electron. In the above, $\mathbf{r}$ and ω are the emitter position vector and frequency, ω_L is the excitation frequency, $\mathcal{E}_F$ is the Fermi energy, ρ_e is the electron density of states, and $\mathbf{E}_L$ is the local field. $|\vec{\mu}(\mathcal{E}_f,\ \mathcal{E}_i)|$ is the transition dipole moment between electronic states with an initial energy $\mathcal{E}_i$ and final energy $\mathcal{E}_f$ (assumed to be energy-independent) and $\rho_{\mathrm{phot}}(\mathbf{r},\ \omega)$ is the local density of photonic states (LDOPS).

https://doi.org/10.1021/acsnano.5c02977
ACS Nano 2025, 19, 29181−29194

The electronic contribution of the emission formula (eq 2) was shown in ref 12 to consist of a series of Planck's blackbody radiation-like terms ($\mathcal{E}_{BB}$), i.e.,

$$I_e(\omega,\ \omega_L,\ |\mathbf{E}_L(\omega_L,\ \mathbf{r})|^2) \sim I_e(\omega,\ \omega_L,\ T_e,\ |\mathbf{E}_L(\omega_L,\ \mathbf{r})|^2) \sim \langle \mathcal{E}_{BB}(\omega;\ T_e)\rangle + 2\langle \mathcal{E}_{BB}(\omega - \omega_L;\ T_e)\rangle \delta_E + \langle \mathcal{E}_{BB}(\omega - 2\omega_L;\ T_e)\rangle \delta_E^2 + \cdots \quad (4)$$

where $\langle \mathcal{E}_{BB}(\omega,\ T_e)\rangle = \hbar\omega/(e^{\hbar\omega/k_B T_e} - 1)$ and

$$\delta_E(\mathbf{r};\ \omega_L,\ \mathrm{pol}',\ \hat{k}') = p_{abs}(\mathbf{r};\ \omega_L,\ \mathrm{pol}',\ \hat{k}')/p_{sat} \quad (5)$$

Here, T_e is the (effective) electron temperature, extracted from the first energy moment of the electron distribution;[40,41,46,47] for CW illumination, the latter is nearly equal to the phonon temperature; however, because the PL literature is inconsistent on the matter, the notation adopted in this manuscript emphasizes that the dependence is on the electron temperature. Furthermore, the absorbed power density (p_{abs}) is defined in terms of the local $\mathbf{E}_L(\mathbf{r};\ \omega_L,\ \mathrm{pol}',\ \hat{k}')$ as

$$p_{abs}(\mathbf{r};\ \omega_L,\ \mathrm{pol}',\ \hat{k}') = \frac{\omega_L \epsilon_0}{2}\epsilon_m''(\omega_L)|\mathbf{E}_L(\mathbf{r};\ \omega_L,\ \mathrm{pol}',\ \hat{k}')|^2 = \alpha_{abs}(\mathbf{r};\ \omega_L,\ \mathrm{pol}',\ \hat{k}')I_{in}(\mathbf{r};\ \omega_L,\ \mathrm{pol}',\ \hat{k}') \quad (6)$$

where $\alpha_{abs}(\mathbf{r};\ \omega_L,\ \mathrm{pol}',\ \hat{k}')$ is the absorption cross-section density or, in more general terms, the absorbed power density per unit incident intensity (I_{in}) of polarization pol′ and incidence direction $\hat{k}'$ at a position $\mathbf{r}$ corresponding to the illumination frequency. The saturation power density can be approximated by[12,41]

$$p_{sat}(\omega_L) = \frac{3}{4}\frac{n_e(\hbar\omega_L)^2}{\mathcal{E}_F \tau_{e-e}} \quad (7)$$

where n_e is the electron density and τ_{e-e} is an average rate of collisions between electrons. For simplicity, we set τ_{e-e} in eq 7 to a value typical for a nonthermal electron, that is, we use the Fermi Liquid theory expression[40,48] at $\mathcal{E} \sim \mathcal{E}_F + \hbar\omega$.

The first term on the RHS of eq 4 represents the average energy of thermal emission per electromagnetic mode (i.e., for vacuum electric fields); the next terms represent the nonthermal emission caused by deviations of the electron distribution from thermal equilibrium due to one photon absorption (1PA), two photon absorption (2PA), etc. As discussed in,[12,35] for CW illumination, these terms are typically small compared to the thermal emission at mid-IR frequencies but dominate the emission close to the illumination frequencies and above them.[12,35] All of these details are depicted in the schematic representation (Figure 1). The complete step structure of the nonthermal contributions was observed experimentally for CW illumination for the first time in ref 18.

Notably, the emission (eq 1) is assumed to occur only within the conduction band, that is, to involve only intraband transitions; in that sense, strictly speaking, α_{abs} should include only the intraband contribution (as in ref 37). This would not matter for the illustrative examples below, for which we study Ag nanostructures, but could somewhat affect the match

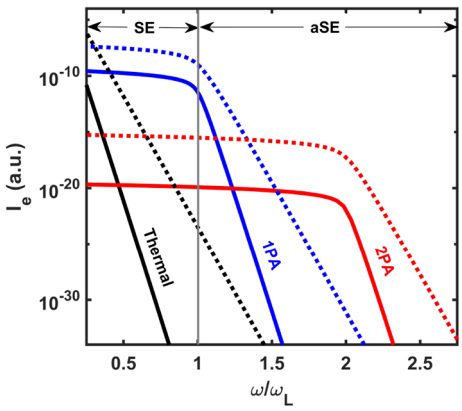

Figure 1. (Color online) Schematic of the contribution from thermal emission: $\langle \mathcal{E}_{BB}(\omega;\ T_e)\rangle$ (black), 1PA: $2\langle \mathcal{E}_{BB}(\omega - \omega_L;\ T_e)\rangle \delta_E$ (blue), 2PA: $\langle \mathcal{E}_{BB}(\omega - 2\omega_L;\ T_e)\rangle \delta_E^2$ (red) from eq 4 calculated under CW wave illumination. The plots are shown for two intensities, where solid and dotted lines indicate lower and higher intensities, respectively.

between our predictions and the experimental data (Sections 3.1.4 and 3.2.3). In order to include interband absorption and emission transitions, our PL formula can be amended by accounting for the increased number of nonthermal holes above the interband absorption threshold in the electron distribution function f, as shown in Figure S10(b) of ref 29, and adding the valence bands to the electron density of states. As shown below, our analysis provides a qualitative (and usually also a quantitative) match to the experimental data even without accounting for these additional transitions.

2.2. A Macroscopic View. The result (eq 1) applies for a general point within the metal. It was so far used to understand the general parametric dependence of the PL on the electric field, its statistics, etc. with only a phenomenological address of the shape and size of the emitting nanostructure.

In order to account for a specific nanostructure geometry, one needs to sum over the random spontaneous emission events from the nanostructure volume as a function of the space. This should allow one to account also for the *actual* magnitude of the emission, thus, including also the portion of the emitted photons that got reabsorbed (sometimes referred to as recycled), rather than only the *probability* of emission (as given by Γ^{em} (eq 1)). This can be done using the local Kirchhoff Law for nonisothermal bodies[49−51] and its extension to metals having nonequilibrium electron distributions.[37] The latter study showed that the actual emitted power in the direction $\hat{k}$ into a solid angle dΩ ($=\frac{d^3k}{k^2 dk}$; see eq (9.15.9) in ref 52) is given by

$$dP^{em}(\omega,\ \omega_L,\ \hat{k}) \cong \frac{\rho_{phot}^{(0)}}{8\pi}\sum_{pol=s,p}\int_V \alpha_{abs}(\mathbf{r};\ \omega,\ \mathrm{pol},\ -\hat{k})\, I_e(\omega,\ \omega_L,\ T_e(\mathbf{r}),\ |\mathbf{E}_L(\mathbf{r};\ \omega_L,\ \mathrm{pol}',\ \hat{k}')|^2) d^3r d\omega d\Omega \quad (8)$$

where $\rho_{phot}^{(0)} = \frac{\omega^2}{\pi^2 c^2}$ is the photonic density of states of free space, pol and pol′ are the polarization of the emitted and incident waves, respectively, and $\alpha_{abs}(\mathbf{r};\ \omega,\ \mathrm{pol},\ -\hat{k})$ is the emission cross-section density (aka emissivity density), which

https://doi.org/10.1021/acsnano.5c02977
ACS Nano 2025, 19, 29181−29194

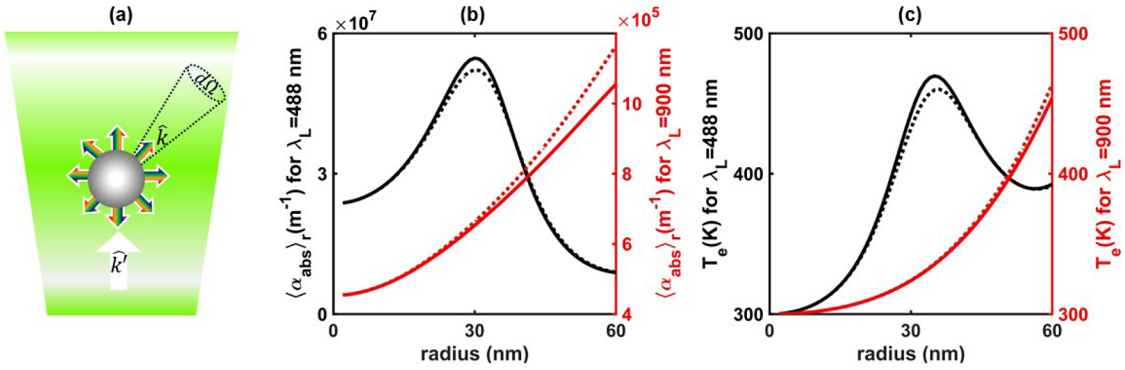

Figure 2. (Color online) (a) A schematic illustration of light emission from a sphere. (b) The absorption cross-section density $\langle\alpha_{abs}\rangle_r$ vs radius for λ_L = 488 nm (black) and 900 nm (red) for Ag spheres in oil. The corresponding illumination intensities are I_{in} = 0.25 MW/cm^2 (black line) and I_{in} = 3.5 MW/cm^2 (red line). The thermo-optic effect on $\langle\alpha_{abs}\rangle_r$ and T_e is represented by the dotted lines. (c) The corresponding (electron) temperature reached due to CW illumination of the Ag spheres, calculated by using eq 11.

by the local Kirchhoff Law, equals the absorption cross-section density. In that regard, following,[49−51] and unlike in ref 37, where the PL was expressed in terms of absorption cross-section, eq 8 utilizes the absorption cross-section density to extend the formulation to structures with nonuniform field distributions.

Using eqs 4−6 in eq 8 gives

$$dP^{em}(\omega,\ \omega_L,\ \hat{k}) \sim \frac{\omega^2}{8\pi^3 c^2} \sum_{pol=s,p} \int_V \left[\frac{I_{in}}{p_{sat}} \alpha_{abs}(\mathbf{r};\ \omega,\ pol,\ -\hat{k}) \alpha_{abs}(\mathbf{r};\ \omega_L,\ pol',\ \hat{k}') 2\langle \mathcal{E}_{BB}(\omega-\omega_L;\ T_e)\rangle_r + \frac{I_{in}^2}{p_{sat}^2} \alpha_{abs}(\mathbf{r};\ \omega,\ pol,\ -\hat{k}) \alpha_{abs}^2(\mathbf{r};\ \omega_L,\ pol',\ \hat{k}') \langle \mathcal{E}_{BB}(\omega-2\omega_L;\ T_e)\rangle_r + \cdots \right] d^3r d\omega d\Omega \quad (9)$$

Eq 9 shows that the quantities that determine the emission are the absorption cross-sectional density α_{abs} and the (electron) temperature distribution. This dependence is similar to that provided in ref 53, as well as to the scaling of surface-enhanced Raman Scattering (see ref 54), but goes beyond these theories by providing a rigorous (rather than an empiric[53]) account of the effect of the electron distribution to the PL. As shown below, the expression (eq 9) also circumvents the more advanced yet complicated k-space calculations (as e.g., in refs 29,30,33), without compromising much predictive capabilities.

We now note that spatially integrated emission (eq 9) involves space-varying functions. Specifically, the spatial distribution of α_{abs} is determined by the material constituents and the geometry of the nanostructure. In addition to gradients induced by illumination nonuniformity (e.g., when a focused beam illuminates a film), equation (eq 9) exhibits significant gradients on scales exceeding the penetration (skin) depth, that is, for more than a few tens of nm for noble metals. In contrast, the nonuniformity of temperature is typically much weaker than that of the electric field (and hence α_{abs}) due to the strong (electron, hence) heat diffusion in metals. This (electron) temperature nonuniformity should, in principle, be extracted from a self-consistent solution of microscopic equations for the electron dynamics; however, in practice, since the deviation from thermal equilibrium is minute for CW illumination,[40,41,45] it is usually determined by coarse-graining such equations into heat equations, see, for example,[40,41,47,55] The resulting single or two temperature models reveal that heat gradients and electron−phonon temperature differences are very small (see, e.g., refs 56−61). Finally, like the absorption cross-section density α_{abs} and unlike the electron temperature T_e, the nonthermal part of the electron distribution, manifested via δ_E (eq 5), is roughly determined by the local electric field distribution. As predicted in refs 31,62 and demonstrated experimentally in ref 29, the reason for that is the minimal (few nm) mean free path of these electrons, which in turn, originates from their femtosecond-scale collision rate. Accordingly, to determine the spatial dependence of the PL integrand, in what follows we use heat equations to determine the electron temperature and rely on the solution of Maxwell's equations to determine the electric field and, hence, α_{abs} and δ_E. Having said that, in many cases (specifically, for few nanometer spheres and uniformly illuminated thin films, both studied below), α_{abs} is quite uniform. In such cases, α_{abs} can be estimated from measurable quantities like the absorption cross-section, σ_{abs} (in the case of particles) or absorptance, A (in the case of films), thus simplifying the formulation slightly and making the analysis of the PL simpler.

3. RESULTS

3.1. Nanospheres under CW Illumination. *3.1.1. Determination of the Electron Temperature.* We start our analysis by considering the PL from nanospheres under CW plane wave illumination in a uniform optical and thermal environment (oil, in our case); see Figure 2a. We choose silver as a prototypical plasmonic material, as it does not require accounting for interband transitions for illumination with visible light. As mentioned above, in this case, it is customary to neglect the small difference between the electron and phonon temperatures (see, e.g., refs 40,41,63) and consider a single temperature model. Nevertheless, as mentioned, we choose to denote the temperature below as T_e, in order to emphasize that it is the electron temperature that is the relevant quantity as far as photon emission in the visible and near-infrared spectral regimes is concerned. Then, the steady-state temperature $T_e(\mathbf{r})$ can be obtained by solving the heat diffusion equation[64]

https://doi.org/10.1021/acsnano.5c02977
ACS Nano 2025, 19, 29181−29194

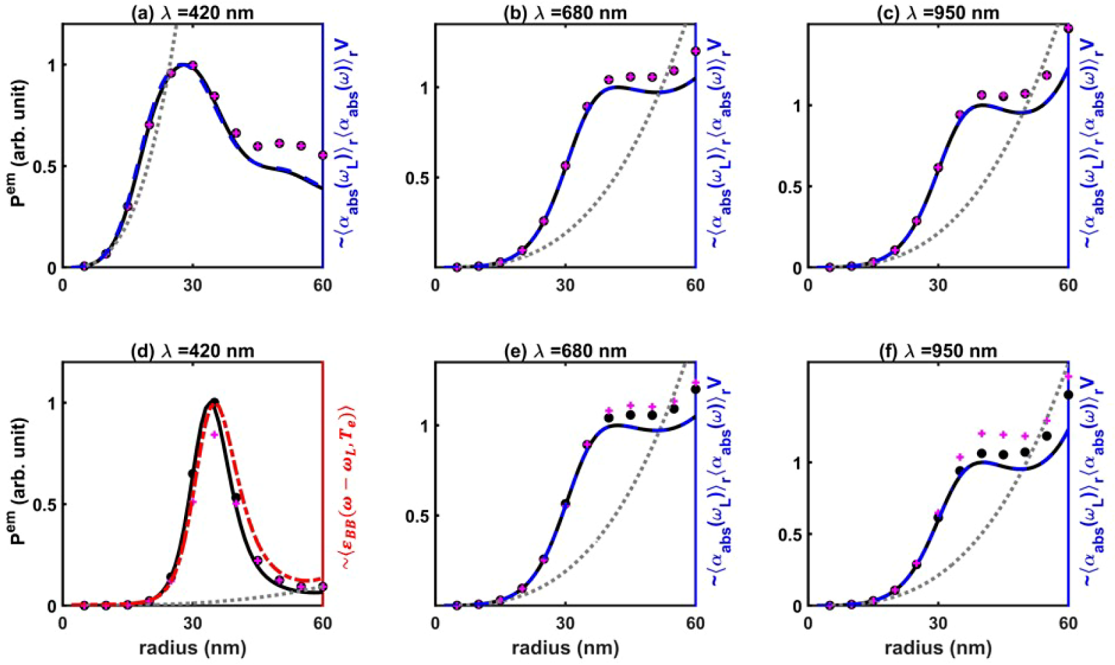

Figure 3. (Color online) The total PL (eq 9; circles) and its homogenized approximation (eq 12; black continuous line) calculated for spheres under CW illumination with λ_L = 488 nm and emission wavelengths of λ = 420 nm ((a) and (d)), λ = 680 nm ((b) and (e)) and λ = 950 nm ((c) and (f)). For these calculations, $p_{sat} \sim 1.2 \times 10^{25}$ W/m^3 and I_{in} used for the calculation are (a)−(c) 2.5 kW/cm^2 and (d)−(f) 0.25 MW/cm^2. The magenta crosses show the PL calculation when the thermo-optic effect is included. The dashed blue lines represent $a^3\langle\alpha_{abs}(\lambda_L)\rangle_r\langle\alpha_{abs}(\lambda)\rangle_r$ and the red dash-dot lines represent $\langle\mathcal{E}_{BB}\rangle$. The gray dotted lines are an a^3 fit to the calculation for a < 10 nm. Frequency and wavelength are used interchangeably, as convenient.

$$\nabla\cdot[\kappa(\mathbf{r})\nabla T_e(\mathbf{r},\ \omega_L)] = \begin{cases} -\alpha_{abs}(\mathbf{r};\ \omega_L)I_{in}, & \text{inside the nanostructure,} \\ 0, & \text{outside the nanostructure} \end{cases} \quad (10)$$

where κ is the thermal conductivity and we used eq 6 on the right-hand-side. Due to the symmetry, $\alpha_{abs}(\mathbf{r};\ \omega_L)$ for a nanosphere is independent of the direction and polarization of the incident beam.

As shown already in refs 36,64, even in the presence of substantial field nonuniformity (occurring for nanospheres of more than a few tens of nm in size), the high thermal conductivity of the metal ensures that the temperature of the nanosphere is only weakly inhomogeneous. In fact, as shown in ref 36, the temperature can be calculated quite accurately also when replacing $\alpha_{abs}(\mathbf{r};\ \omega_L)$ in eq 10 by its spatial average, $\langle\alpha_{abs}(\mathbf{r};\ \omega_L)\rangle_r = \frac{1}{V}\int\alpha_{abs}(\mathbf{r};\ \omega_L)d\mathbf{r} = \sigma_{abs}(\omega_L)/V$. Particularly, for spheres whose radius is up to ≈ 60 nm, the temperature can be approximated as

$$T_e \approx \langle T_e\rangle_r = T_h + \frac{\langle\alpha_{abs}(\mathbf{r};\ \omega_L)\rangle_r I_{in}}{3\kappa_h}a^2 \quad (11)$$

Here, κ_h and T_h are the thermal conductivity and temperature of the surrounding media far from the particle.

As a representative example, Figure 2b,c show $\langle\alpha_{abs}(\mathbf{r};\ \omega_L)\rangle_r$ and the (electron) temperature (eq 11), respectively, calculated for Ag spheres of sizes up to 60 nm dispersed in oil (permittivity ϵ_h = 2.235, thermal conductivity k_h = 0.2873 Wm^{-1}K^{-1}) for an excitation laser wavelength λ_L close to the (dipolar) plasmon resonance (488 nm) and for a wavelength farther from the resonance (900 nm), where permittivity of Ag is set to −9.12 + 1.45i and − 45.11 + 3.60i, respectively. The absorption cross-section (density) is well studied,[65] hence, described below only briefly. Specifically, $\langle\alpha_{abs}$ $(\mathbf{r};\ \lambda_L$ = 488 nm$)\rangle_r$ shows a peak at around 30 nm. For a < 10 nm, the absorption cross-section $\sigma_{abs}(\omega_L)$ (hence, $\langle\alpha_{abs}(\mathbf{r};\ \omega_L)\rangle_r \sim \sigma_{abs}(\omega_L)/a^3$) takes the quasi-static form, $\sigma_{abs}^{qs} \simeq \frac{6\pi}{\lambda}V\Im\left(\frac{\epsilon-\epsilon_{bg}}{\epsilon+2\epsilon_{bg}}\right)$ (see Figure S1 or more generally,[65]). As the sphere radius increases, the $\lambda \sim$ 400 nm dipole resonance undergoes a red-shift (see Figure S2a). Thus, since the chosen excitation wavelength $\lambda_L \sim$ 488 nm is at the long wavelength tail of the resonance, $\langle\alpha_{abs}(\mathbf{r};\ \omega_L)\rangle_r$ increases with a as the dipole resonance tunes toward λ_L. However, the strength of the dipole resonance decreases with growing sphere size, so that beyond a ∼ 30 nm the importance of higher-order resonances increases, and thus, the absorption becomes limited to the surface. The corresponding size dependence of σ_{abs} is shown in Figure S1.

Similarly, for excitation at λ_L = 900 nm, the averaged absorption cross-section density $\langle\alpha_{abs}\rangle_r$ increases monotonically with the sphere size for all sizes studied here since the peak response occurs beyond the range of consideration in this work, see Figure S1b. In that sense, the off-resonance illumination case behaves as in the small size regime of the on-resonance case; we will not dwell on it further in this study.

Figure 2c shows the corresponding size-dependence of the electron temperature. By eq 11, and as explained in ref 36, the size-dependence of the temperature T_e originates from the proportionality with $\langle\alpha_{abs}(\mathbf{r};\ \omega_L)\rangle_r$ and a^2. Specifically, for on-resonance excitation, the product $\langle\alpha_{abs}(\mathbf{r};\ \omega_L)\rangle_r a^2$ results in a peak of T_e at ≈35 nm while for off-resonance excitation, the monotonic increase of $\langle\alpha_{abs}(\mathbf{r};\ \omega_L)\rangle_r$ results in a monotonic increase of T_e. The similarity to the size-dependence of the absorption cross-section density is apparent.

https://doi.org/10.1021/acsnano.5c02977
ACS Nano 2025, 19, 29181−29194

3.1.2. Determination of the PL. Figure 3 illustrates the size-dependence of the total PL (as per eq 9) for an excitation wavelength close to resonance (λ_L = 488 nm). The intensities used for the calculations are chosen such that at the lower intensity (I_{in} = 2.5 kW /cm^2), the temperature of each sphere is close to room temperature and at the higher intensity (I_{in} = 0.25 MW /cm^2) the maximum temperature does not exceed 500 K (for which sintering and damage may start to occur). The calculations are conducted at three different emission wavelengths. The calculated emission at λ = 420 nm (aSE; Figure 3a) displays a peak at a = 28 nm when excited by the low intensity. When excited at a higher intensity (Figure 3d), the peak slightly red-shifts to a = 34 nm and becomes more distinct. For the emission at λ = 680 nm (SE; Figure 3b,e), the PL increases monotonously until $a \approx$ 42 nm, decreases until a = 51 nm, and then rises again. The PL at λ = 950 nm, (lower frequency SE; Figure 3c,f) exhibits a similar behavior, except for a higher slope beyond a = 50 nm.

As already noted above, the expression for PL (eq 9) can be further simplified for a sphere. As discussed in Section 3.1.1, the temperature is fairly uniform in the sphere, and the space-dependence of I_e in eq 9 originates only from that of α_{abs} and δ_E, as indicated by eq 4. Furthermore, we rely on the calculations of the mean free path of the nonthermal electrons[31] to justify the neglect of spatial broadening of the nonthermal electron distribution. These results motivate the use of the analytical result (eq 4) also for nonuniform fields, that is to approximate the level of nonthermal electron population δ_E by simply summing over its local value across the particle volume. Accordingly, δ_E (eq 5) can be expressed in terms of the spatially averaged, $\langle\alpha_{abs}(\mathbf{r};\ \omega_L)\rangle_r$. With this consideration, I_e (eq 4) becomes independent of the position. The volume integration over $\alpha_{abs}(\mathbf{r};\ \omega)$ is now replaceable by the absorption cross-section of the sphere, which in turn, can be expressed as $\sigma_{abs}(\omega) \sim a^3\langle\alpha_{abs}(\mathbf{r};\ \omega)\rangle_r$. Thus, eq 9 simplifies to

$$\mathrm{d}P^{em}(\omega,\ \omega_L) \sim \omega^2 a^3 \langle\alpha_{abs}(\mathbf{r};\ \omega)\rangle_r \left[2\frac{I_{in}}{p_{sat}(\omega_L)}\langle\alpha_{abs}(\mathbf{r};\ \omega_L)\rangle_r\langle\mathcal{E}_{BB}(\omega-\omega_L;\ T_e)\rangle_r + \left(\frac{I_{in}}{p_{sat}(\omega_L)}\right)^2\langle\alpha_{abs}(\mathbf{r};\ \omega_L)\rangle_r^2\langle\mathcal{E}_{BB}(\omega-2\omega_L;\ T_e)\rangle_r\right] \mathrm{d}\omega\mathrm{d}\Omega \quad (12)$$

Using this expression, we can determine the total PL solely via the absorption cross-section density evaluated at the pump frequency ($\langle\alpha_{abs}(\mathbf{r};\ \omega_L)\rangle_r$, Figure 2b) and emission frequency ($\langle\alpha_{abs}(\mathbf{r};\ \omega)\rangle_r$, Figure S2a), as well as the electron temperature (Figure 2c). As seen in Figure 3a–c, the qualitative behavior of the PL (eq 9) and its approximation (eq 12) is nearly identical except for the former being slightly higher for a > 30 nm.

While the computational simplification associated with eq 12 is minor, its more significant contribution is to allow us to pinpoint the origins of the behavior observed in Figure 3. Specifically, the PL in Figure 3a–c pertains roughly to room temperature for all sphere sizes, making the Bose function ($\mathcal{E}_{BB}(\omega-\omega_L)$) essentially size-independent. In this scenario, the PL varies with sphere size as the product of $\langle\alpha_{abs}(\mathbf{r};\ \omega_L)\rangle_r$ (at the absorption wavelength), $\langle\alpha_{abs}(\mathbf{r};\ \omega)\rangle_r$ (at the emission wavelength) and the volume, V. For spheres of radius a < 10 nm (i.e., safely within the quasi-static regime), $\langle\alpha_{abs}\rangle_r$ has a very weak dependence on the volume (see Figure S1) so that the PL scales as a^3. For spheres with sufficiently large radii with respect to the skin depth, the absorption is dominated by the surface layer of the particle so that $\langle\alpha_{abs}\rangle_r \sim 1/a$. Consequently, the PL scales linearly with a ($\sim a^3\frac{1}{a}\frac{1}{a}$). For sphere sizes between these two extremes, the subvolume scaling of the absorption and temperature, along with variations in $\langle\alpha_{abs}\rangle_r$ with particle size owing to the sphere's modal response (see ref 36 and Figure 2b) result in the observed deviation from the volume scaling, namely, the peaks and troughs in the PL shown in all subplots of Figure 3. Specifically, the nonmonotonic behavior in the PL observed for the larger sizes is due to the combined effect of the system tuning into and then out of the dipole resonance and then tuning into the quadrupole mode. In that respect, considering the PL as being a volume effect for small spheres and as a surface effect for larger spheres is a crude description, which misses the dominant effect of the modal structure but captures the baseline.

Figure 3d–f shows the PL for a higher intensity which results in a size-dependent temperature, varying from room temperature to ∼500 K (see Figure 2c). The higher varying temperature affects the different parts of the PL spectrum. First, it hardly affects the SE (Figure 3e,f) which thus follows the same trend observed for the low-intensities, at least up to temperatures for which thermo-optic effects are still negligible[39,66] (see Section 3.1.3 below). Indeed, for SE, the nonthermal contribution from the 1PA term dominates I_e (see eq 4, Figures 1 and S3), which is nearly temperature-independent since it originates from the nonthermal electron shoulders given in eq 5 (see SI Section S3 of ref 12). In contrast, the aSE is exponentially sensitive to the temperature via the Bose function $\langle\mathcal{E}_{BB}(\omega-\omega_L;\ T_e)\rangle$ (see Figure 1). As a result, the size-dependence of the PL is much stronger (Figure 3d), exhibiting superlinear scaling with the volume.

Deeper into the aSE regime, the 2PA term becomes stronger than the 1PA term; see Figure 1. To demonstrate this, we calculate the PL for a longer (off-resonant) excitation wavelength (900 nm, i.e., smaller ω_L), see Figure S4. In this case, while the near aSE (Figure S4b,e) grows as $\langle\alpha_{abs}(\mathbf{r};\ \omega_L)\rangle_r$, for frequencies sufficiently deep into the aSE, the PL scales as $\sim\langle\alpha_{abs}(\mathbf{r};\ \omega_L)\rangle_r^2$ at low intensity excitation (Figure S4a) and as $\sim\langle\mathcal{E}_{BB}(\omega-2\omega_L)\rangle$ at high intensity illumination (Figure S4d).

Finally, in order to show the generality of our approach, and to demonstrate that the behavior we identify is not qualitatively affected by the choice of the exciting laser frequency (e.g., its position with respect to resonance), we replicate the results of Figure 3 (for which the illumination is on the red-side of the plasmon resonance) in Figures S5 and S6 for backgrounds with higher refractive indices. This results in a red-shift of the resonances and introduces the higher-order modal response to the PL emission, particularly for the larger spheres. However, the qualitative behavior is similar to that with the lower background refractive index.

3.1.3. The Thermo-Optic Effect. Illumination at high intensity can induce significant changes in the temperature of the spheres, consequently altering their permittivity via the so-called thermo-optic effect,[38,67,68] and as a result, modify the absorptivity (hence, the emissivity) and finally the PL. To analyze this effect, we assume that the permittivity of the metal

https://doi.org/10.1021/acsnano.5c02977
ACS Nano 2025, 19, 29181–29194

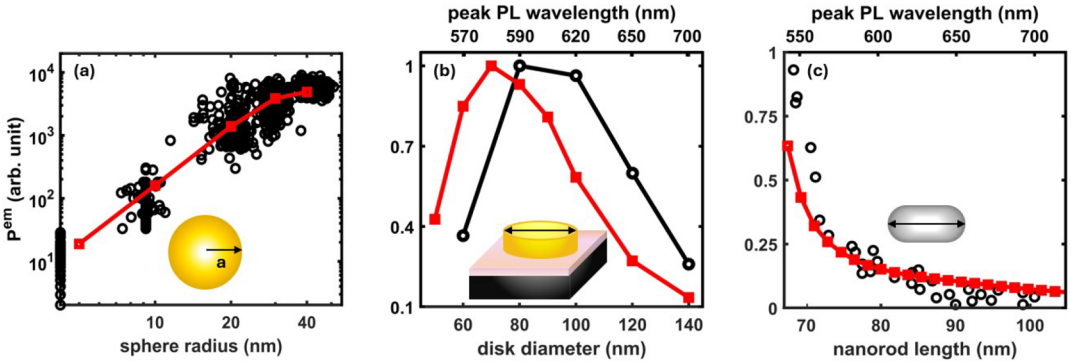

Figure 4. (Color online) (a) Normalized PL from gold spheres on a glass substrate immersed in glycerol with λ_L = 514 nm with emission integrated over the range of 560−640 nm, as measured by Gaiduk et al.[25] (b) PL spectrally resolved peak positions and intensities vs diameter of gold disks of height 30 nm at λ_L = 532 nm as measured by Hu et al.[26] (c) Spectrally integrated PL from silver nanorods of diameter 23 nm on a quartz substrate, at λ_L = 532 nm as measured by Lin et al.[28] In all panels, experimental results and theoretical calculations using eq 9 are depicted by black circles and red squares, respectively, with the corresponding solid lines added for visual guidance. The corresponding calculated PL peak positions are indicated on the top axis of (b) and (c).

and the thermal conductivity of the surrounding medium depend linearly on the change of temperature, compute the thermo-derivative of the metal permittivity from ellipsometry data[69] and set the thermo-derivative of the thermal conductivity of the surrounding medium to 1.3×10^{-4} $Wm^{1-}K^{-2}$, as in ref 66 the temperature of the nanoparticle is then calculated using the method described by Un and Sivan.[66]

Overall, as the intensity (hence, temperature) increases, the real part of the permittivity (ϵ_m') becomes more negative, while the imaginary part (ϵ_m'') increases to higher positive values at most frequencies. This results in a blue shift of the resonance peak and a broadening of its spectral width, leading to enhanced absorption at off-resonance frequencies, see Figure S7 and refs 38,68−71. As a result, $\langle \alpha_{abs}(\mathbf{r}; \omega) \rangle_r$ slightly decreases at 488 nm and slightly increases at 900 nm, as seen in Figure 2b. The decrease in the former case leads to a reduction in the temperature for the hottest spheres (around a = 30 nm), and hence, to the reduction of the aSE observed in Figure 3d. However, the SE PL is hardly affected by the temperature. Thus, the increase in $\langle \alpha_{abs}(\mathbf{r}; \omega) \rangle_r$ at longer wavelengths results in a slight increase of the PL, as observed in Figure 3e,f. For excitation at 900 nm, the temperature of the spheres (especially for a > 30 nm) increases slightly compared to the value calculated for the linear case, leading to a slight increase in the PL for aSE, as shown in Figure S4d,e. The thermo-optic increase of $\langle \alpha_{abs}(\mathbf{r}; \omega_L) \rangle_r$ and $\langle \alpha_{abs}(\mathbf{r}; \omega) \rangle_r$ leads to a slight increase in SE, as observed in Figure S4f.

3.1.4. Comparison to Single-Particle Experiments. Our theoretical predictions can be compared to various single particle PL measurements. First, Figure 4a shows that our calculations align with the experimental observations of the normalized SE PL (spectrally integrated over the range of 560−640 nm) measured from single gold nanospheres of different sizes, as reported by Gaiduk et al. (see Figure S5 of ref 25). The experimental results are presented as they appear in the referenced paper (in arbitrary units), and the corresponding theoretical calculations are scaled by a constant normalization factor to enable a quantitative comparison with the experimental data. In this experiment, the illumination intensity was adjusted to keep the temperature rise relatively low (approximately below 20 K). The PL is calculated using eq 9 with the refractive index of gold obtained from ref 72, and those of glass and glycerol being 1.45 and 1.47, respectively. The normalized PL roughly scales with the volume until $a \sim$ 30 nm but seems to saturate upon further increase in size; assuming this is the onset of a decrease, this is in line with our prediction.

Size-dependence of the PL from larger particles was studied by Hu et al.[26] who demonstrated that the spectral peak of the PL from gold nanodisks on a SiO_2-coated absorptive (silicon) substrate initially increases, reaches a maximum, and then decreases significantly with further increases in size. The absorption cross-section densities and the T_e of the disks are calculated using COMSOL, considering normal incidence and emission perpendicular to the substrate, with the permittivity data for gold and Si taken from ref 72 and ref 73, respectively. Calculations based on eq 9 exhibit a qualitatively similar trend (even if at a slight spectral shift).

Finally, our theoretical prediction of PL is compared with the PL measurements by Lin et al.[28] This work showed the spectrally integrated PL from single nanorods of different lengths with constant diameter along their main axis. In contrast to the nanospheres (and in similarity to films, shown later), the PL monotonically decreases with the nanorod length. These results are reproduced in Figure 4c along with the theoretical prediction, that is, the spectral integration of eq 9. The optical response is calculated in COMSOL, where the substrate refractive index is n = 1.45 and the permittivity of the silver rods is taken from ref 72. The temperature is estimated with an approximate expression[64] and remains close to the ambient temperature (0.1% variation) for the laser illumination intensity considered (I_{in} = 3 mW/cm^2). Good qualitative agreement is obtained for nanorods longer than 72 nm; however, our prediction underestimates the PL for shorter nanorods, thus providing only a qualitative match for this regime (specifically, in a 30 nm wide wavelength range close to the pump). A similar observation was recently reported above the pump wavelength for Au rods;[37] in that case, the discrepancy between theory and measurements was ascribed to interband transitions.

Remarkably, while our theory (eq 9) includes only emission events occurring in the conduction band, it successfully predicts the dependence of the emission on the particle size even in spectral regimes where interband emission events should occur (specifically, for the spheres and nanodisks (Figure 4a,b, respectively). This implies that, in these cases,

https://doi.org/10.1021/acsnano.5c02977
ACS Nano 2025, 19, 29181−29194

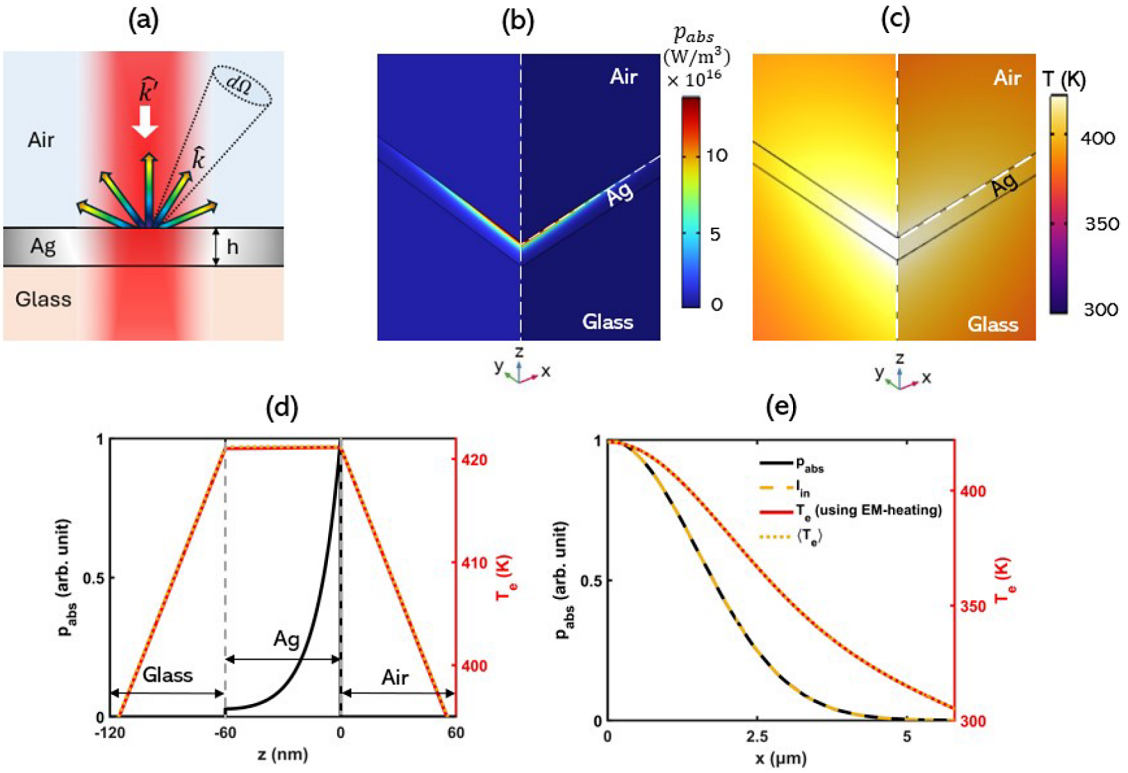

Figure 5. (Color online) (a) Schematic illustration of the emission from an Ag film on a glass substrate illuminated from above by a focused Gaussian beam. (b) The absorbed power density calculated for a 60 nm film due to continuous wave illumination at a wavelength of 488 nm, using the electromagnetic heating module of COMSOL Multiphysics (shown on a quarter domain). (c) The corresponding calculated temperature distribution. (d) Vertical (along the *z*-axis) and (e) transverse (*x*-axis, $z = 0$) cross sections of the absorbed power density and temperature. The red-solid and yellow dotted lines in (d) and (e) represent T_e calculated using eq 10, considering the actual distribution of $\alpha_{abs}(\mathbf{r}; \omega_L)$ and the position averaged $\langle \alpha_{abs}(\mathbf{r}; \omega_L)\rangle_z$ respectively. The yellow dashed line in (e) represents the distribution of the incident intensity along the *x*-axis. The peak intensity and radius of illumination are 2 MW/cm^2 and 3 μm, respectively.

interband transitions modify the emission features in a modest quantitative manner, but not qualitatively. We expect that inclusion of such transitions may yield a better quantitative match to the experimental results, due to a better match of the permittivity and nonthermal electron distribution.

3.2. Films under Continuous Illumination. We now turn to studying the PL from a thin film of a Drude metal using the approach used above. Specifically, we examine a thin silver film on a glass substrate illuminated at normal incidence (hence, no dependence on polarization pol′, and $k_z = |k'|$, where k_z is the component of the wavenumber **k** normal to the surface of the film) by a focused Gaussian CW beam with an intensity profile $I_{in}(\rho, \omega_L) = I_0 e^{-2\rho^2/b^2}$ as depicted in Figure 5a.

3.2.1. Determination of the Electron Temperature. The absorbed power density and temperature distribution calculated by solving the heat eq 10 using the electromagnetic heat module of COMSOL Multiphysics are presented in Figure 5b,c, respectively, for excitation at a wavelength of 488 nm. The absorbed power density decreases exponentially along the illumination direction (*z*-axis) due to the short penetration depth (Figure 5d). However, along the radius, it exhibits nearly the same distribution as that of the incident intensity, as shown in Figure 5e.

In contrast, the temperature variation across the film's thickness is minimal (see Figure 5d) due to the high thermal conductivity of the metal; for the same reason, along the radius, the temperature shows a Gaussian profile with a full width at half-maximum (fwhm) greater than that of the incident beam, as illustrated in Figure 5e.

Generically, $\alpha_{abs}(\mathbf{r}; \omega_L, \text{pol}', \hat{k}')$ is uniform in the plane of the film (i.e., it is independent of ρ and ϕ) and varies only along the thickness of the film (i.e., it is only *z*-dependent). The average value of $\alpha_{abs}(z, \omega_L, \text{pol}', \hat{k}')$ along the thickness can be derived from the experimentally measurable quantity, the absorptance $A(\omega, \text{pol}', \hat{k}')$, as

$$\begin{aligned}\langle \alpha_{abs}(z,\ \omega_L,\ \text{pol}',\ \hat{k}')\rangle_z &= \frac{1}{h}\int_h \alpha_{abs}(z,\ \omega_L,\ \text{pol}',\ \hat{k}')\mathrm{d}z \\ &= \frac{A(\omega_L,\ \text{pol}',\ \hat{k}')}{h}\end{aligned} \tag{13}$$

$\alpha_{abs}(\mathbf{r}; \omega_L, \text{pol}', \hat{k}')$ and its average can also be calculated using the transfer matrix method.[74] For normal incidence, this quantity is independent of the polarization.

Because the variation of temperature along the film thickness is negligible (see Figure 5c,d), the temperature of the film can be calculated by using the *z*-averaged cross-section density $\langle \alpha_{abs}(z, \omega_L, \text{pol}', \hat{k}')\rangle_z$ in eq 10. The temperature calculated for a 60 nm Ag film with this approximation closely matches the temperature calculated based on the exact absorbed power density distribution, as shown in Figure 5e. This also enables simplifying the expression for the PL in eq 9 by separating the

https://doi.org/10.1021/acsnano.5c02977
ACS Nano 2025, 19, 29181−29194

integrations with respect to z and ρ, as discussed in more detail in Section 3.2.2.

The size-dependence of $\langle\alpha_{abs}(z;\omega_L)\rangle_z$ for normal incidence at λ_L = 488 and 900 nm are shown in Figure 6a. $\langle\alpha_{abs}(z,\omega_L)\rangle_z$

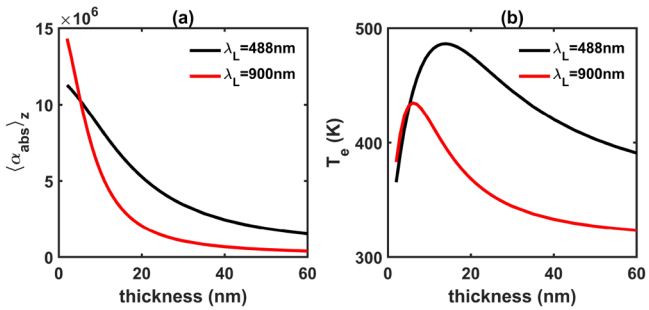

Figure 6. (Color online) (a) $\langle\alpha_{abs}\rangle_z$ and (b) the (electron) temperature of Ag films at the center of the illumination by a CW Gaussian beam with central intensity I_0 = 1.5 MW/cm^2 and b = 3 μm, with λ_L = 488 nm (black) and λ_L = 900 nm (red).

decreases with increasing film thickness for both wavelengths with this decay occurring more rapidly at the longer wavelength. This trend can be explained by the distribution of the electric field within the metal film. Typically, the electric field is strongest near the surface of the metal film and exhibits an exponential decay as it penetrates deeper into the material. Thus, as the film thickness increases, the average field and, hence, absorptance density A/h decreases. This decay is more rapid for λ = 900 nm due to its shorter penetration depth (= 21 nm) compared to the penetration depth of 26 nm at λ_L = 488 nm as shown in Figures 6a and S2b.

Unlike the case of spheres, the size-dependence of the film temperature differs from α_{abs}. The temperature at the center of the illumination spot (ρ = 0) as a function of film thickness is depicted in Figure 6b. Maximal temperature is reached at h = 14 and 6 nm, corresponding to the short and long wavelengths, respectively. This peak temperature can be explained from Fourier's law of heat transfer (solution of the divergence in eq 10), according to which, $T_e \propto h\langle\alpha_{abs}(z;\omega_L)\rangle_z$. Thus, with an increasing thickness, the temperature initially increases. However, due to the sharp decline of $\langle\alpha_{abs}(\mathbf{r};\omega_L)\rangle_r$, with thickness, the temperature eventually decreases, resulting in a peak.

3.2.2. Determination of the PL. Figure 7 presents the predicted PL obtained using eq 9 for Ag films of thickness ranging from 2 to 60 nm. For this calculation, we consider normal illumination at a wavelength of 488 nm, with the emitted PL collected within a solid angle, $d\Omega$ positioned directly above the illumination point. As above, calculations are performed at two incident intensities: one for which the films remain roughly at room temperature (I_0 = 1.5 kW/cm^2) and the other to elevate their temperature to 486 K (I_0 = 1.5 MW/cm^2) as shown in Figure 6b. At room temperature, the PL at the three emission wavelengths (420, 680, and 950 nm) shows peaks at film thicknesses of 13, 8, and 6 nm, respectively. Similar to the case of the spheres, when the peak illumination intensity is increased to I_0 = 1.5 MW/cm^2, the trends of SE remain unchanged so that Figure 7e,f are hardly distinguishable from Figure 7b,c. However, the peak corresponding to the aSE becomes narrower.

Similar to the analysis of the PL from particles above, the PL can be again approximated by replacing $\alpha_{abs}(z)$ by its average value along the thickness, $\langle\alpha_{abs}(z)\rangle_z$ as

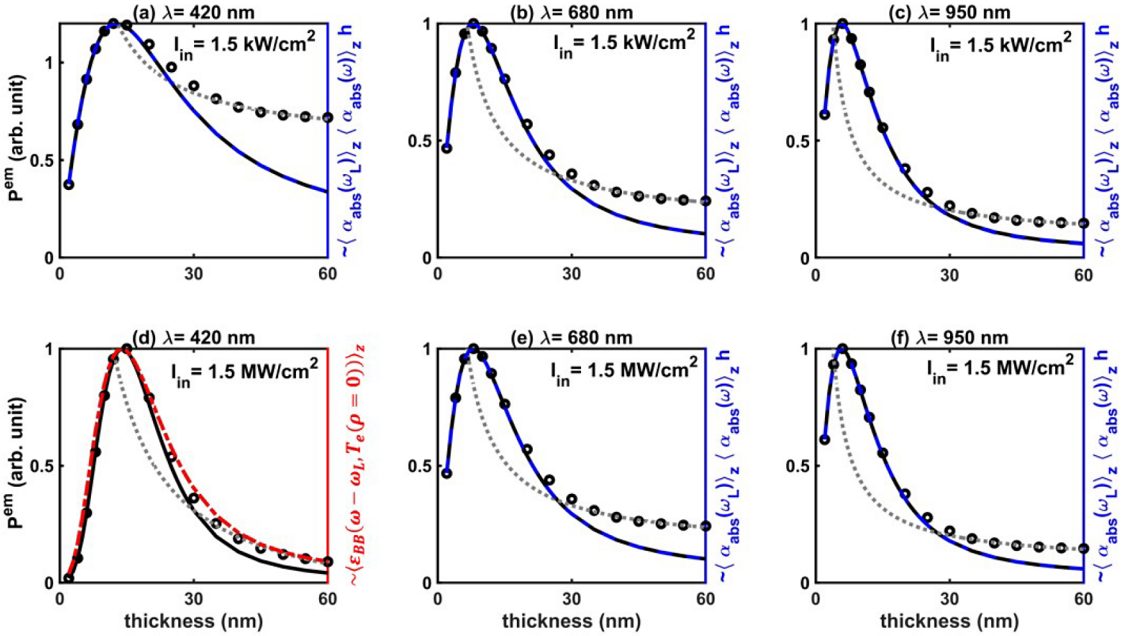

Figure 7. (Color online) The total PL calculated for the films using eq 9 (circles) and that using uniform field approximation (black continuous line) under CW illumination with λ_L = 488 nm and emission wavelengths of λ = 420 nm ((a) and (d)), λ = 680 nm ((b) and (e)) and λ = 950 nm ((c) and (f)). For these calculations, $p_{sat} \sim 1.2 \times 10^{25}$ W/m^3 and I_0 values are (a)−(c) 1.5 kW/cm^2 and (d)−(f) 1.5 MW/cm^2. The dashed blue lines represent $\langle\alpha_{abs}(\omega_L)\rangle_z\langle\alpha_{abs}(\omega)\rangle_z h$ and the red dash-dot lines represent $\langle\mathcal{E}_{BB}\rangle$ at ρ = 0. The gray dotted lines represent a $1/h$ fit to the calculations for h > 30 nm.

https://doi.org/10.1021/acsnano.5c02977
ACS Nano 2025, 19, 29181−29194

$$dP^{em}(\omega,\ \omega_L,\ \hat{k}) \sim \sum_{pol=s,p} \frac{\omega^2}{4\pi^2 c^2}\left[\frac{1}{p_{sat}(\omega_L)}\right.$$
$$\left(h\langle\alpha_{abs}(z,\ \omega_L)\rangle_z\langle\alpha_{abs}(z,\ \omega)\rangle_z \int_{\rho=0}^{\infty} 2I_{in}(\rho,\ \omega_L)\right.$$
$$\left.\langle\mathcal{E}_{BB}(\omega-\omega_L;\ T_e(\rho))\rangle_z \rho d\rho\right) + \frac{1}{p_{sat}^2(\omega_L)}$$
$$\left(h\langle\alpha_{abs}^2(z,\ \omega_L)\rangle_z\langle\alpha_{abs}(z,\ \omega)\rangle_z \int_{\rho=0}^{\infty} I_{in}^2(\rho,\ \omega_L)\right.$$
$$\left.\left.\langle\mathcal{E}_{BB}(\omega-2\omega_L;\ T_e(\rho))\rangle_z \rho d\rho\right)\right] d\omega d\Omega \quad (14)$$

Again, the calculations (eq 14) closely match the results with the exact calculations (eq 9), with the SE (Figure 7b,c,e,f) and low temperature aSE (Figure 7a) being well approximated by $\langle\alpha_{abs}(z,\ \omega_L)\rangle_z\langle\alpha_{abs}(z,\ \omega)\rangle_z h$ for films up to $h \sim 20$ nm, after which the approximation falls below the exact results.

As for particles, we can now deduce the general scaling of the PL with the size from eq 14. Specifically, for very thin films ($h < 5$ nm), $\langle\alpha_{abs}(z)\rangle_z$ decays relatively slowly. As a result, due to the presence of the h term in the PL expression in eq 14, the PL in this regime exhibits sublinear growth. For thicker films ($h > 30$ nm), $\alpha_{abs}(z)\rangle_z \sim 1/h$ is due to the fact that total absorption becomes almost independent of film thickness ($\int\alpha_{abs}dz = \text{Const}$). Consequently, the PL scales as $\frac{1}{h}\frac{1}{h}h = 1/h$, as demonstrated in Figure 7. In the intermediate region, a peak appears. The stronger decay of $\langle\alpha_{abs}(z)\rangle_z$ at longer wavelengths causes the PL peak to shift slightly toward smaller values of h (see Figures 7c,f and S8). As seen in Figure 7d, for higher temperatures, the aSE undergoes exponential amplification via the $\langle\mathcal{E}_{BB}(\omega-\omega_L;\ T_e(\rho))\rangle_z$ term, resulting in sharper peaks compared to those at the room temperature.

The PL calculated at a longer excitation wavelength of 900 nm allows us to explore the PL behavior deeper into the aSE regime, where the 2PA contribution takes over the 1PA contribution, see Figure S8a,d. For this excitation wavelength, while the PL in the near aSE region (Figure S8b,e) can be explained using the same reasoning applied to $\lambda_L = 488$ nm illustrated in Figure 7a,d, in the deeper aSE regime, the PL varies as $\sim\langle\alpha_{abs}(z,\ \omega_L)\rangle_z^2$ (rather than $\langle\alpha_{abs}(z,\ \omega_L)\rangle_z$) at room temperature and as $\sim\langle\mathcal{E}_{BB}(\omega-2\omega_L,\ T_e(\rho))\rangle_z$ (rather than $\langle\mathcal{E}_{BB}(\omega-\omega_L,\ T_e(\rho))\rangle_z$) at the high temperature excitation. It should be noted that, in the high-temperature 2PA aSE case shown in Figure S8d, $\langle\mathcal{E}_{BB}(\omega-\omega_L,\ T_e(\rho))\rangle_z$ overestimates the exact calculation (eq 9) due to the additional dependence of the exact PL on $\langle\alpha_{abs}(z,\ \omega_L)\rangle_z^2$. As the temperature increases further, $\langle\mathcal{E}_{BB}(\omega-\omega_L,\ T_e(\rho))\rangle_z$ provides a closer estimate of the exact PL.

Note that unlike the case of particles, the PL from the film decreases monotonically beyond the increase for small sizes. The reason for that is the absence of the resonances that occur for particles, into which the system is tuning in and out with varying size.

3.2.3. Comparison to Experiments. As previously done for single particles, we now compare the predictions of our simple analytical PL formula to recent experimental measurements. Specifically, we look at Figures 3a−c and S20a,b of Bowman et al.,[29] which presents PL measurements from single crystal Au films of various thicknesses. Only a few film thicknesses were studied, but data are available for several emission frequencies (rather than for single frequencies, as for particles). The PL recorded for the individual films is shown in Figure 8,

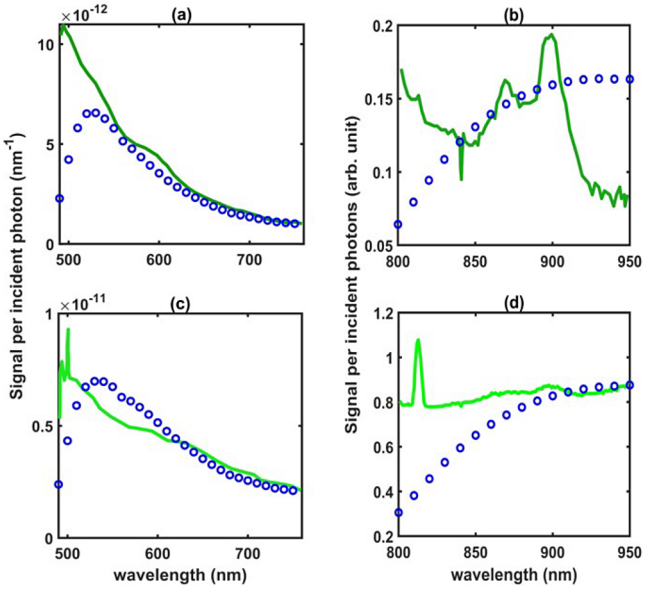

Figure 8. (Color online) The recorded PL signal (number of emitted photons, solid lines) per incident photon per emission wavelength for film thicknesses (a), (b) h = 33.3 nm and (c), (d) h = 13.4 nm, taken from Figures 3a and S20a of Bowman et al.,[29] shown alongside our calculations (circles). Data of (a) and (c) is given in units nm^{-1} *multiplied by a constant factor of 8* for excitation wavelength of λ_L = 488 nm with I_{in} = 0.162 mW/μm^2 and the data of (b) and (d) is given in arbitrary units multiplied by a constant factor of 6 × 10^{13} for λ_L = 785 nm with I_{in} = 1.87 mW/μm^2. In these calculations, the PL is integrated over a solid angle, with the emission angle ranging from 0 to 44° corresponding to the numerical aperture of the objective lens used in the experiment.

alongside our calculations. To conform with the data of the original paper, our results for λ_L = 488 nm (Figure 8a,c) are given in units of nm^{-1} (as in Figure 3a−c of ref 29, multiplied by a constant factor of 8), while those for λ_L = 785 nm (Figure 8b,d) are presented in arbitrary units (as in Figure S20a of ref 29, and are normalized using a method analogous to that employed for the experimental results of spheres shown in Figure 4a. For 488 nm excitation, the calculated results tend to fall below the experimental data at shorter wavelengths. This discrepancy likely arises from the omission of interband contributions in our emission calculations.

In order to remove the impact of instrumental noise and a substrate-related Raman peak, we follow[29] and show the PL ratio spectra for the same films (i.e., the PL data/difference normalized by the data from a thick film) which are presented in Figures 3c and S20b from Bowman et al.[29] in Figure 9a,c and b,d, respectively, along with our own theoretical prediction for films (eq 9). For the 488 nm excitation, *despite* the differences observed at short wavelengths in Figure 8a,c, our calculations now closely match the theoretical results of Bowman et al.[29] for all thicknesses studied (see results for the thicker films inFigure S9). A similar match can be observed for 785 nm excitation as well (Figure 9b,d). In fact, our theoretical predictions match the more sophisticated theory of[29] even in

https://doi.org/10.1021/acsnano.5c02977
ACS Nano 2025, 19, 29181−29194

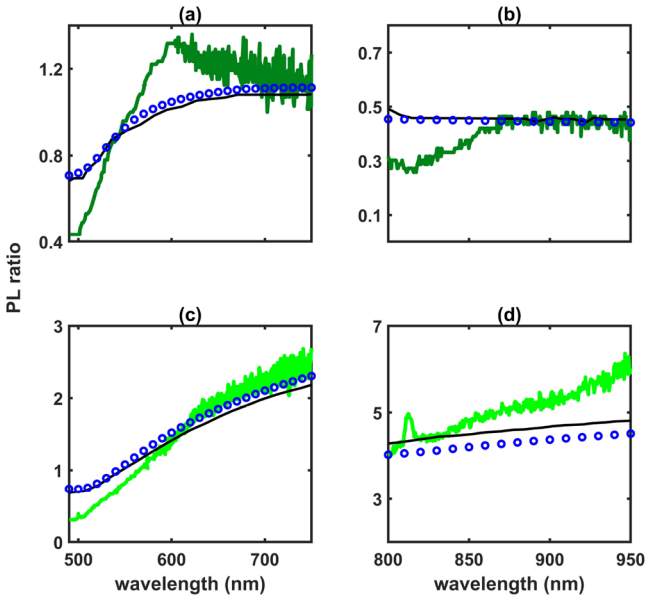

Figure 9. (Color online) Corresponding PL ratios experimental (colored solid lines) and simulation (black solid lines) results for the PL from golds films of thickness (a), (b) h = 33.3 nm and (c), (d) h = 13.4 nm to that of a thicker film (h = 113 nm for (a) and (c) and h = 88 nm for (b) and (d)), taken from Figures 3c and S20b of Bowman et al.[29] They are compared to our calculation (eq 9) shown as blue circles. Panels (a) and (c) show the ratio $\frac{\mathrm{PL}(h)}{\mathrm{PL}(h=113\ \mathrm{nm})}$ as a function of emission wavelength, using excitation conditions of λ_L = 488 nm, and panels (b) and (d) display the normalized difference $\frac{\mathrm{PL}(h)-\mathrm{PL}(h=88\ \mathrm{nm})}{\mathrm{PL}(h=25.8\ \mathrm{nm})-\mathrm{PL}(h=88\ \mathrm{nm})}$ at λ_L = 785 nm.

the parts of the spectra where the latter does not match the experimental data well, leaving the discrepancies unexplained by either theoretical approach. This is remarkable, since the theory in ref 29 involved the summation of the individual dipole emissions, a treatment of the electron states as a discrete set in momentum space, and a detailed DFT-based calculation of the permittivity. Those we replaced by the local Kirchhoff Law, empiric permittivity data, and our simple analytical formula for the PL (eq 9) were based on a continuous set of energy states, along with standard macroscopic electromagnetic and thermal calculations. Thus, overall, the quantitative match for the normalized data implies that the contribution of interband transitions to the PL exhibits a size dependence very similar to the intraband transition-based prediction.

4. CONCLUSIONS

In this work, we provide a unifying explanation for the dependence of PL from metal nanostructures on their size. Specifically, using the experimentally established expression for the nonequilibrium electron distribution in the conduction band,[40,41,43−45] together with recent extension of the local Kirchhoff Law for light emission from metals characterized this nonequilibrium electron distribution,[37] we provide a simple analytical form for the (intensity, temperature and) size-dependence of the PL. In particular, we show that the size-dependence of the Stokes emission (SE) is determined primarily by the size-dependence of the absorption (= emission) cross-section density (aka emissivity density) but that the aSE is much more sensitive to the structure size at high illumination intensities due to the exponential dependence of the Bose function $\langle \mathcal{E}_{BB}(\omega, T_e)\rangle$ on the electron temperature T_e.

This behavior is illustrated schematically in Figure 10. As seen, generically, the PL from particles and films grows for

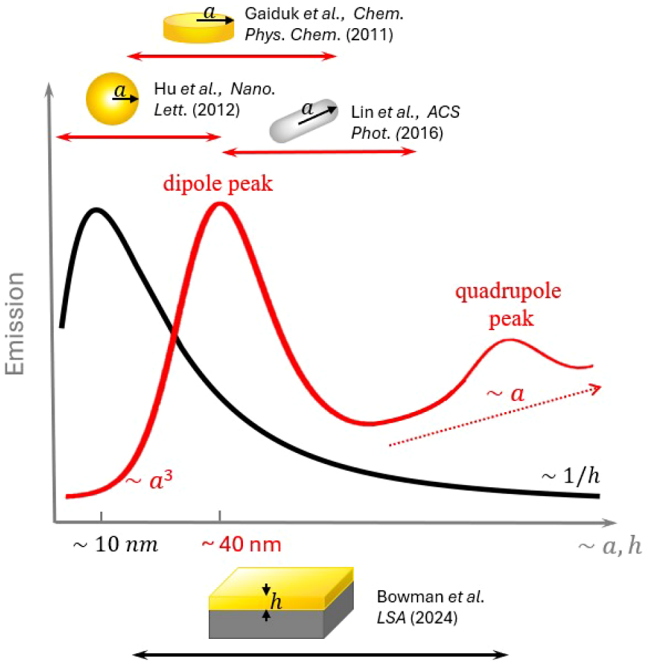

Figure 10. (Color online) Schematic summary of the size dependence of the PL from the structures studied in this work.

small sizes as the volume/thickness, respectively, and then decreases due to the decrease of the average local field (or equivalently, of the emissivity). The size for which maximal PL is attained is found to be larger for particles than for films (~30 nm vs ~10 nm, respectively, for illumination near resonance; the maximal size is higher for off-resonant illumination). This explains the seemingly contradicting trends observed in experiments (e.g., refs 17,24,25) - they originate from the fact that measurements from thin films[17,29] were so far performed only for films thicker than the size of maximal PL (>10 nm), most likely, because thinner films tend to be discontinuous (i.e., below the percolation limit). A similar behavior was observed for rods. Once advanced fabrication of sub 10 nm thick films will be employed for (CW) PL studies (as, e.g., in ref 17), the quantum effects predicted in ref 29 could be identified. Notably, the trends described in Figure 10 apply both for spectrally resolved and spectrally integrated PL; moreover, the trends will be qualitatively similar also for different wavelengths, for higher temperatures/intensities, and for the aSE, in which cases, the sensitivity to the size will be greater.

Our predictions were shown to match well a range of experimental results of SE, including for cases that formally lie beyond the limits of validity of the analysis, including nonspherical particles and their arrays. The quantitative discrepancies observed in some cases may originate in differences in the underlying permittivity data, in subtleties associated with the significant field nonuniformity in this case, or in missing elements needed for a complete description of the PL, for example, the inclusion of emission originating from inelastic electron scattering (which should dominate the

https://doi.org/10.1021/acsnano.5c02977
ACS Nano 2025, 19, 29181−29194

emission near the pump frequencyh[33]), interband transitions and the subtle QM effects highlighted in ref 29. Even better understanding of these discrepancies may be obtained by comparing to aSE measurements, which were so far done in the context of thermometry,[6−9] but not done systematically as a function of the structure size.

Our analytical approach provides a very simple alternative to the highly complicated rigorous (discrete *k*-space) calculations of the PL offered in some recent studies.[29,30,33] In particular, the use of the extension of the local Kirchhoff Law to nonequilibrium electron distributions[37] allows circumventing many of the detailed electromagnetic emission calculations done in ref 29 and validates the approximations we made, e.g., the neglect of the energy-dependence of the matrix elements and electron density of states; this finding is in line with the good agreement obtained when matching our theoretical approach to measurement of currents in molecular and current junctions.[42−45] Moreover, while the analytical expression we provide accounts only for intraband transitions, it is found to yield good qualitative and sometimes even quantitative agreement with experimental data from Au nanostructures in regimes for which interband emission was shown to be significant. In this context, the modeling of the contribution of interband transitions to the PL in ref 18 should be questioned, especially since it is based on an unjustified 100−fold reduction of the electron−phonon coupling coefficient.

Nevertheless, while both the rigorous *k*-space approach and our approximate analytic approaches are capable of reproducing most aspects of the experimental observations, the current study highlights the ability of the more rigorous approaches to capture subtle aspects of the emission such as the determination of the conditions under which the emission is due to radiative recombination or inelastic scattering (see, e.g., discussions in refs 5,29,33,75−79) or emission from prescattered electrons.[29] Similarly, while the only quantum aspect of our theory is the use of the quantum version of the Boltzmann equation (see ref 40), while the electron states themselves (and thus, the permittivity) and the photon properties do not involve quantization, the more rigorous *k*-space approach should allow identifying subtle quantum mechanical effects that go beyond the standard quantum size effect (e.g.,[80,81]) such as the thickness dependence of the CW PL from atomic flat metal films (see Figure 4a of ref 29) and in the future, maybe even the high sensitivity to the number of atomic levels observed in ref 17 for the PL due to pulsed illumination.

While in the current work we focused on the PL from simple structures and noble metals, our approach can be applied also to more complicated structures for which the local electric field is even more nonuniform such as long rods,[82] various particle dimers,[33,82−84] trimers[85] etc., or to other plasmonic materials, including low electron density Drude materials such as transparent conducting oxides.[86,87] We also emphasize that the analysis in the current manuscript is limited to CW illumination, but could be extended also to pulsed illumination.[10,11,17,21,88] In this scenario, which was studied more extensively in the past, the size-dependence of the temperature is different, and there is a dynamic transition between the nonthermal and thermal parts (see[35]), which entails further complexity. This class of experiments will be analyzed separately in future work. Ultimately, our work paves the way to the simple optimization of the PL for practical purposes.

5. METHODS/EXPERIMENTAL

Methods used in the manuscript include standard numerical simulations using a commercial software (COMSOL Multiphysics).

ASSOCIATED CONTENT

Supporting Information

The Supporting Information is available free of charge at https://pubs.acs.org/doi/10.1021/acsnano.5c02977.

Absorption cross-section of spheres, absorption characteristics across spectrum, thermal and nonthermal contribution to PL of sphere, PL of sphere excited off-resonance, PL calculated for higher order mode responses, the thermo-optic effect on absorption, PL calculation for films (ZIP)

AUTHOR INFORMATION

Corresponding Author

Yonatan Sivan − *School of Electrical and Computer Engineering, Ben-Gurion University of the Negev, Beer Sheva 8410501, Israel*; Email: sivanyon@bgu.ac.il

Authors

Imon Kalyan − *School of Electrical and Computer Engineering, Ben-Gurion University of the Negev, Beer Sheva 8410501, Israel*

Ieng Wai Un − *Guangdong Basic Research Center of Excellence for Structure and Fundamental Interactions of Matter, School of Physics and Guangdong-Hong Kong Joint Laboratory of Quantum Matter, South China Normal University, Guangzhou 510006, China*; orcid.org/0000-0002-7156-0019

Gilles Rosolen − *Micro and Nanophotonic Materials Group, Research Institute for Materials Science and Engineering, University of Mons, 7000 Mons, Belgium*; orcid.org/0000-0002-7399-3838

Nir Shitrit − *School of Electrical and Computer Engineering, Ben-Gurion University of the Negev, Beer Sheva 8410501, Israel*; orcid.org/0000-0003-2929-9707

Complete contact information is available at: https://pubs.acs.org/10.1021/acsnano.5c02977

Notes

The authors declare no competing financial interest.

ACKNOWLEDGMENTS

I.K. and Y.S. were partially funded by Israel Science Foundation (ISF) grant no. 340/2020, a Lower-Saxony-Israel collaboration grant no. 76251-99-7/20 (ZN 3637) as well as a grant from the Bronitzki family. I.W.U. was funded by the Guangdong Natural Science Foundation (Grants No. 2024A1515011457).

REFERENCES

(1) Wolfbeis, O. S. An overview of nanoparticles commonly used in fluorescent bioimaging. *Chem. Soc. Rev.* **2015**, *44*, 4743−4768.

(2) He, H.; Xie, C.; Ren, J. Nonbleaching Fluorescence of Gold Nanoparticles and Its Applications in Cancer Cell Imaging. *Anal. Chem.* **2008**, *80*, 5951−5957.

(3) Li, W.; Schierle, G. S. K.; Lei, B.; Liu, Y.; Kaminski, C. F. Fluorescent Nanoparticles for Super-Resolution Imaging. *Chem. Rev.* **2022**, *122*, 12495−12543.

(4) Perkovic, M.; Kunz, M.; Endesfelder, U.; Bunse, S.; Wigge, C.; Yu, Z.; Hodirnau, V. V.; Scheffer, M. P.; Seybert, A.; Malkusch, S.;

Schuman, E. M.; Heilemann, M.; Frangakis, A. S. Correlative Light- and Electron Microscopy with chemical tags. *J. Struct. Bio.* **2014**, *186*, 205−213.
(5) Hugall, J. T.; Baumberg, J. J. Demonstrating Photoluminescence from Au is Electronic Inelastic Light Scattering of a Plasmonic Metal: The Origin of SERS Backgrounds. *Nano Lett.* **2015**, *15*, 2600−2604.
(6) Xie, X.; Cahill, D. G. Thermometry of Plasmonic Nanostructures by Anti-Stokes Electronic Raman Scattering. *Appl. Phys. Lett.* **2016**, *109*, 183104.
(7) Carattino, A.; Caldarola, M.; Orrit, M. Gold Nanoparticles as Absolute Nano-Thermometers. *Nano Lett.* **2018**, *18*, 874−880.
(8) Jones, S.; André, D.; Karpinski, P.; Käll, M. Photothermal Heating of Plasmonic Nanoantennas: Influence on Trapped Particle Dynamics and Colloid Distribution. *ACS Photonics* **2018**, *5*, 2878−2887.
(9) Jollans, T.; Caldarola, M.; Sivan, Y.; Orrit, M. Effective Electron Temperature Measurement Using Time-Resolved Anti-Stokes Photoluminescence. *J. Phys. Chem. A* **2020**, *124*, 6968−6976.
(10) Beversluis, M.; Bouhelier, A.; Novotny, L. Continuum Generation from Single Gold Nanostructures through Near-Field Mediated Intraband Transitions. *Phys. Rev. B* **2003**, *68*, No. 115433.
(11) Roloff, L.; Klemm, P.; Gronwald, I.; Huber, R.; Lupton, J. M.; Bange, S. Light Emission from Gold Nanoparticles under Ultrafast Near-Infrared Excitation: Thermal Radiation, Inelastic Light Scattering, or Multiphoton Luminescence? *Nano Lett.* **2017**, *17*, 7914−7919.
(12) Sivan, Y.; Dubi, Y. Theory of "Hot" Photoluminescence from Drude Metals. *ACS Nano* **2021**, *15*, 8724−8732.
(13) Mooradian, A. Photoluminescence of Metals. *Phys. Rev. Lett.* **1969**, *22*, 185.
(14) Boyd, G. T.; Yu, Z. H.; Shen, Y. R. Photoinduced Luminescence from the Noble Metals and Its Enhancement on Roughened Surfaces. *Phys. Rev. B* **1986**, *33*, 7923.
(15) Ghenuche, P.; Cherukulappurath, S.; Taminiau, T. H.; van Hulst, N. F.; Quidant, R. Spectroscopic Mode Mapping of Resonant Plasmon Nanoantennas. *Phys. Rev. Lett.* **2008**, *101*, No. 116805.
(16) Shahbazyan, T. V. Theory of Plasmon-Enhanced Metal Photoluminescence. *Nano Lett.* **2013**, *13*, 194−198.
(17) Grossmann, S.; Friedrich, D.; Karolak, M.; Kullock, R.; Krauss, E.; Emmerling, M.; Sangiovanni, G.; Hecht, B. Nonclassical Optical Properties of Mesoscopic Gold. *Phys. Rev. Lett.* **2019**, *122*, No. 246802.
(18) Lee, A.; Wu, S.; Yim, J. E.; Zhao, B.; Sheldon, M. T. Hot Electrons in a Steady State: Interband vs. Intraband Excitation of Plasmonic Gold. *ACS Nano* **2024**, *18*, 19077−19085.
(19) Cai, Y.-Y.; Sung, E.; Zhang, R.; Tauzin, L. J.; Liu, J. G.; Ostovar, B.; Zhang, Y.; Chang, W.-S.; Nordlander, P.; Link, S. Anti-Stokes Emission from Hot Carriers in Gold Nanorods. *Nano Lett.* **2019**, *19*, 1067−1073.
(20) Huang, J.; Wang, W.; Murphy, C. J.; Cahill, D. G. Resonant Secondary Light Emission from Plasmonic Au Nanostructures at High Electron Temperatures Created by Pulsed-Laser Excitation. *Proc. Nat. Acad. Sci. U.S.A* **2014**, *111*, 906−911.
(21) Haug, T.; Klemm, P.; Bange, S.; Lupton, J. M. Hot-Electron Intraband Luminescence from Single Hot Spots in Noble-Metal Nanoparticle Films. *Phys. Rev. Lett.* **2015**, *115*, No. 067403.
(22) Liu, J. G.; Zhang, H.; Link, S.; Nordlander, P. Relaxation of Plasmon-Induced Hot Carriers. *ACS Photonics* **2018**, *5*, 2584−2595.
(23) Ai, Q.; Zhang, H.; Wang, J.; Giessen, H. Multiphoton Photoluminescence in Hybrid Plasmon-Fiber Cavities with Au and Au@Pd Nanobipyramids: Two-Photon vs. Four-Photon Processes and Rapid Quenching. *ACS Photonics* **2021**, *8*, 2088.
(24) Dulkeith, E.; Niedereichholz, T.; Klar, T. A.; Feldmann, J.; von Plessen, G.; Gittins, D. I.; Mayya, K. S.; Caruso, F. Plasmon Emission in Photoexcited Gold Nanoparticles. *Phys. Rev. B* **2004**, *70*, No. 205424.
(25) Gaiduk, A.; Yorulmaz, M.; Orrit, M. Correlated absorption and photoluminescence of single gold nanoparticles. *ChemPhysChem* **2011**, *12*, 1536−1541.
(26) Hu, H.; Duan, H.; Yang, J. K. W.; Shen, Z. X. Plasmon-Modulated Photoluminescence of Individual Gold Nanostructures. *ACS Nano* **2012**, *6*, 10147−10155.
(27) Zheng, J.; Zhou, C.; Yu, M.; Liu, J. Different sized luminescent gold nanoparticles. *Nanoscale* **2012**, *4*, 4073.
(28) Lin, K.-Q.; Yi, J.; Hu, S.; Sun, J.-J.; Zheng, J.-T.; Wang, X.; Ren, B. Intraband Hot-Electron Photoluminescence from Single Silver Nanorods. *ACS Photonics* **2016**, *3*, 1248−1255.
(29) Bowman, A. R.; Echarri, A. R.; Kiani, F.; Iyikanat, F.; Tsoulos, T. V.; Cox, J. D.; Sundararaman, R.; de Abajo, F. J. G.; Tagliabue, G. Quantum-mechanical effects in photoluminescence from thin crystalline gold films. *Light: Sci. Appl.* **2024**, *13*, 91.
(30) Echarri, A. R.; Iyikanat, F.; Boroviks, S.; Mortensen, N. A.; Cox, J. D.; de Abajo, F. J. G. Nonlinear photoluminescence in gold thin films. *ACS Photonics* **2023**, *10*, 2918−2929.
(31) Brown, A. M.; Sundararaman, R.; Narang, P.; Goddard, W. A.; Atwater, H. A. Nonradiative Plasmon Decay and Hot Carrier Dynamics: Effects of Phonons, Surfaces, and Geometry. *ACS Nano* **2016**, *10*, 957−966.
(32) Lee, S. A.; Kuhs, C. T.; Searles, E. K.; Everitt, H. O.; Landes, C. F.; Link, S. d-Band Hole Dynamics in Gold Nanoparticles Measured with Time-Resolved Emission Upconversion Microscopy. *Nano Lett.* **2023**, *23*, 3501−3506.
(33) Amoruso, A. B.; Boto, R. A.; Elliot, E.; de Nijs, B.; Esteban, R.; Földes, T.; Aguilar-Galindo, F.; Rosta, E.; Aizpurua, J.; Baumberg, J. J. Uncovering low-frequency vibrations in surface-enhanced Raman of organic molecules. *Nat. Commun.* **2024**, *15*, 6733.
(34) Koopman, W.; Stete, F.; Bargheer, M. Auger-excited Photoluminescence from Gold Nanoflowers. *ChemRXiv* **2024**,
(35) Sivan, Y.; Un, I. W.; Kalyan, I.; Lin, K.; Lupton, J.; Bange, S. Crossover from nonthermal to thermal photoluminescence from metals excited by ultrashort light pulses. *ACS Nano* **2023**, *17*, 11439−11453.
(36) Un, I. W.; Sivan, Y. Size-dependence of the Photothermal Response of a Single Metal Nanosphere. *J. Appl. Phys.* **2019**, *126*, 173103.
(37) Loirette-Pelous, A.; Greffet, J.-J. Theory of photoluminescence by metallic structures. *ACS Nano* **2024**, *18*, 31823−31833.
(38) Sivan, Y.; Chu, S.-W. Nonlinear Plasmonics at High Temperatures. *Nanophotonics* **2017**, *6*, 317−328.
(39) Gurwich, I.; Sivan, Y. A Metal Nanosphere under Intense Continuous Wave Illumination - a Unique Case of Non-Perturbative Nonlinear Nanophotonics. *Phys. Rev. E* **2017**, *96*, No. 012212.
(40) Dubi, Y.; Sivan, Y. "Hot" Electrons in Metallic Nanostructures - Non-Thermal Carriers or Heating? *Light: Sci. Appl.* **2019**, *8*, 89.
(41) Sivan, Y.; Un, I. W.; Dubi, Y. Assistance of Plasmonic Nanostructures to Photocatalysis - Just a Regular Heat Source. *Faraday Discuss.* **2019**, *214*, 215−233.
(42) Reddy, H.; Wang, K.; Kudyshev, Z.; Zhu, L.; Yan, S.; Vezzoli, A.; Higgins, S. J.; Gavini, V.; Boltasseva, A.; Reddy, P.; Shalaev, V. M.; Meyhofer, E. Determining plasmonic hot-carrier energy distributions via single-molecule transport measurements. *Science* **2020**, *369*, 423−426.
(43) Dubi, Y.; Un, I. W.; Sivan, Y. Distinguishing thermal from non-thermal ("hot") carriers in illuminated molecular junctions. *Nano Lett.* **2022**, *5*, 2127−2133.
(44) Février, P.; Basset, J.; Estéve, J.; Aprili, M.; Gabelli, J. Role of optical rectification in photon-assisted tunneling current. *Commun. Phys.* **2023**, *6*, 29.
(45) Lin, C.; Krecinic, F.; Yoshino, H.; Hammud, A.; Pan, A.; Wolf, M.; Müller, M.; Kumagai, T. Continuous-Wave Multiphoton-Induced Electron Transfer in Tunnel Junctions Driven by Intense Plasmonic Fields. *ACS Photonics* **2023**, *10*, 3637−3646.
(46) Pietanza, L. D.; Colonna, G.; Longo, S.; Capitelli, M. Non-Equilibrium Electron and Phonon Dynamics in Metals under Femtosecond Laser Pulses. *Eur. Phys. J. D* **2007**, *45*, 369−389.
(47) Saavedra, J. R. M.; Asenjo-García, A.; de Abajo, F. J. G. Hot-Electron Dynamics and Thermalization in Small Metallic Nanoparticles. *ACS Photonics* **2016**, *3*, 1637−1646.

https://doi.org/10.1021/acsnano.5c02977
ACS Nano 2025, 19, 29181−29194

(48) Coleman, P. *Introduction to many body physics*; Cambridge University Press: Cambridge, 2015.
(49) Greffet, J.-J.; Bouchon, P.; Brucoli, G.; Marquier, F. Light Emission by Nonequilibrium Bodies: Local Kirchhoff Law. *Phys. Rev. X* **2018**, *8*, No. 021008.
(50) Bailly, E.; Chevrier, K.; de la Vega, C. R. P.; Hugonin, J.-P.; Wilde, Y. D.; Krachmalnicoff, V.; Vest, B.; Greffet, J.-J. Method to measure the refractive index for photoluminescence modelling. *Opt. Mater. Express* **2022**, *12*, 2772−2781.
(51) Nguyen, A.; Greffet, J.-J. Efficiency optimization of mid-infrared incandescent sources with time-varying temperature. *Optical Materials Express* **2022**, *12*, 225−239.
(52) Reif, F. *Fundamentals of statistical and thermal physics*; McGraw-Hill Science/Engineering/Math, 1965.
(53) Lin, K.-Q.; Yi, J.; Zhong, J.-H.; Hu, S.; Liu, B.-J.; Liu, J.-Y.; Zong, C.; Lei, Z.-C.; Wang, X.; Aizpurua, J.; Esteban, R.; Ren, B. Plasmonic photoluminescence for recovering native chemical information from surface-enhanced Raman scattering. *Nat. Commun.* **2017**, *8*, 14891.
(54) Khurgin, J. B.; Sun, G.; Soref, R. A. Enhancement of Luminescence Efficiency Using Surface Plasmon Polaritons: Figures of Merit. *J. Opt. Soc. Am. B* **2007**, *24*, 1968−1980.
(55) Fatti, N. D.; Voisin, C.; Achermann, M.; Tzortzakis, S.; Christofilos, D.; Valleé, F. Nonequilibrium electron dynamics in noble metals. *Phys. Rev. B* **2000**, *61*, 16956−16966.
(56) Baffou, G.; Quidant, R. Thermo-plasmonics: Using metallic nanostructures as nano-sources of heat. *Laser Photon. Rev.* **2013**, *7*, 171−187.
(57) Block, A.; Liebel, M.; Yu, R.; Spector, M.; Sivan, Y.; de Abajo, J. G.; van Hulst, N. F. Tracking ultrafast hot-electron diffusion in space and time by ultrafast thermomodulation microscopy. *Sci. Adv.* **2019**, *5*, No. eaav8965.
(58) Sivan, Y.; Spector, M. Ultrafast dynamics of optically heat gratings in metals. *ACS Photonics* **2020**, *7*, 1271−1279.
(59) Gao, G.; Jiang, L.; Xue, B.; Yang, F.; Wang, T.; Wan, Y.; Zhu, T. Unconventional Shrinkage of Hot Electron Distribution in Metal Directly Visualized by Ultrafast Imaging. *Small Methods* **2023**, *7*, No. 2201260.
(60) Block, A.; Yu, R.; Un, I. W.; Varghese, S.; Liebel, M.; van Hulst, N. F.; Fan, S.; Tielrooij, K. Y.; Sivan, Y. Observation of negative effective thermal diffusion in gold films. *ACS Photonics* **2023**, *10*, 1150−1158.
(61) Karna, P.; Hoque, M. S. B.; Thakur, S.; Hopkins, P. E.; Giri, A. Direct Measurement of Ballistic and diffusive Electron Transport in Gold. *Nano Lett.* **2023**, *23*, 491−496.
(62) Bernardi, M.; Mustafa, J.; Neaton, J. B.; Louie, S. G. Theory and computation of hot carriers generated by surface plasmon polaritons in noble metals. *Nat. Commun.* **2015**, *6*, 7044.
(63) Meng, L.; Yu, R.; Qiu, M.; de Abajo, F. J. G. Plasmonic Nano-Oven by Concatenation of Multishell Photothermal Enhancement. *ACS Nano* **2019**, *11*, 7915−7924.
(64) Baffou, G.; Quidant, R.; de Abajo, F. J. G. Nanoscale Control of Optical Heating in Complex Plasmonic Systems. *ACS Nano* **2010**, *4*, 709−716.
(65) Bohren, C. F.; Huffman, D. R. *Absorption and scattering of light by small particles*; Wiley & Sons, 1983.
(66) Un, I. W.; Sivan, Y. The Thermo-Optic Nonlinearity of Single Metal Nanoparticles under Intense Continuous-Wave Illumination. *Phys. Rev. Mater.* **2020**, *4*, No. 105201.
(67) Boyd, R. W. *Nonlinear Optics*, 2nd ed.; Academic Press: San Diego, 2003.
(68) Lee, H.; Im, S.; Lee, C.; Lee, H.; Chu, S.-W.; Ho-Pui, A.; Kim, H. D. Probing Temperature-Induced Plasmonic Nonlinearity: Unveiling Opto-Thermal Effects on Light Absorption and Near-Field Enhancement. *Nano Lett.* **2024**, *6*, 3598−3605.
(69) Reddy, H.; Guler, U.; Chaudhuri, K.; Dutta, A.; Kildishev, A. V.; Shalaev, V. M.; Boltasseva, A. Temperature-Dependent Optical Properties of Single Crystalline and Polycrystalline Silver Thin Films. *ACS Photonics* **2017**, *4*, 1083−1091.
(70) Shen, P.-T.; Sivan, Y.; Lin, C.-W.; Liu, H.-L.; Chang, C.-W.; Chu, S.-W. Temperature- and -roughness dependent permittivity of annealed/unannealed gold films. *Opt. Exp.* **2016**, *24*, 19254.
(71) Reddy, H.; Guler, U.; Kildishev, A. V.; Boltasseva, A.; Shalaev, V. M. Temperature-dependent optical properties of gold thin films. *Optical Materials Express* **2016**, *6*, 2776−2802.
(72) Johnson, P. B.; Christy, R. W. Optical constants of noble metals. *Phys. Rev. B* **1972**, *6*, 4370−4379.
(73) Aspnes, D. E.; Studna, A. A. Dielectric functions and optical parameters of Si, Ge, GaP, GaAs, GaSb, InP, InAs, and InSb from 1.5 to 6.0 eV. *Phys. Rev. B* **1983**, *27*, 985−1009.
(74) Ohta, K.; Ishida, H. Matrix formalism for calculation of electric field intensity of light in stratified multilayered films. *Appl. Opt.* **1990**, *29*, 1952−1959.
(75) Shen, Y. R. Distinction between Resonant Raman Scattering and Hot Luminescence. *Phys. Rev. B* **1974**, *9*, 622−626.
(76) Klein, M. V. Equivalence of Resonance Raman Scattering in Solids with Absorption Followed by Luminescence. *Phys. Rev. B* **1973**, *8*, 919−921.
(77) Solin, J. R.; Merkelo, H. Resonant Scattering or Absorption followed by Emission. *Phys. Rev. B* **1975**, *12*, 624−629.
(78) Solin, J. R.; Merkelo, H. Reply to "Comment on "Resonant Scattering or Absorption Followed by Emission"". *Phys. Rev. B* **1976**, *14*, 1775−1776.
(79) Shen, Y. R. Comment on "Resonant Scattering or Absorption Followed by Emission". *Phys. Rev. B* **1976**, *9*, 1772−1774.
(80) Kreibig, U.; Vollmer, M. *Optical Properties of Metal Clusters*; Springer: Berlin, 1995.
(81) Alvarez, M. M.; Khoury, J. T.; Schaaff, T. G.; Shafigullin, M. N.; Vezmar, I.; Whetten, R. L. Optical Absorption Spectra of Nanocrystal Gold Molecules. *J. Phys. Chem. B* **1997**, *101*, 3706−3712.
(82) Agreda, A.; Sharma, D. K.; Viarbitskaya, S.; Hernandez, R.; Cluzel, B.; Demichel, O.; Weeber, J.-C.; des Francs, G. C.; Kumar, G.; Bouhelier, A. Spatial Distribution of the Nonlinear Photoluminescence in Au Nanowires. *ACS Photonics* **2019**, *6*, 1240−1247.
(83) Huang, D.; Byers, C. P.; Wang, L.-Y.; Hoggard, A.; Hoener, B.; Dominguez-Medina, S.; Chen, S.; Chang, W.-S.; Landes, C. F.; Link, S. Photoluminescence of a Plasmonic Molecule. *ACS Nano* **2015**, *97*, 7072−7079.
(84) Lemasters, R.; Manjare, M.; Freeman, R.; Wang, F.; Pierce, L. G.; Hua, G.; Urazhdin, S.; Harutyunyan, H. Non-thermal emission in gap-mode plasmon photoluminescence. *Nat. Commun.* **2024**, *10*, 4468.
(85) Yin, T.; Dong, Z.; Jiang, L.; Zhang, L.; Hu, H.; Qiu, C.-W.; Yang, J. K. W.; Shen, Z. X. Anomalous Shift Behaviors in the Photoluminescence of Dolmen-Like Plasmonic Nanostructures. *ACS Photonics* **2016**, *3*, 979−984.
(86) Kinsey, N.; DeVault, C.; Boltasseva, A.; Shalaev, V. M. Near-zero-index materials for photonics. *Nat. Rev. Mater.* **2019**, *4*, 742−760.
(87) Un, I. W.; Sarkar, S.; Sivan, Y. An electronic-based model of the optical nonlinearity of low electron density Drude materials. *Phys. Rev. Applied* **2023**, *19*, No. 044043.
(88) Suemoto, T.; Yamanaka, K.; Sugimoto, N. Observation of femtosecond infrared luminescence in gold. *Phys. Rev. B* **2019**, *100*, No. 125405.

https://doi.org/10.1021/acsnano.5c02977
ACS Nano 2025, 19, 29181−29194